

existence of this phase diagram supports the fundamental concept of jamming, and confirms the applicability of jamming to describe the behaviour of attractive particles. However, the shape of the experimental phase diagram differs significantly from that originally proposed by Liu and Nagel², having everywhere the opposite curvature, and diverging at each corner. These divergences reflect the particular details of attractive colloidal particles and correspond to irreversible aggregation, where ϕ_c^{-1} is large; to the limit of hard spheres, where T/U is large; and to high volume fractions of strongly attracting particles that form, for example, sintered solids, where σ_y is large.

The basic concept of a jamming phase transition to describe these diverse phenomena is supported by the similarity in the behaviour as the boundary is crossed; variation in ϕ or U leads to equivalent critical-like behaviour for the viscosity (equations (1) and (3)) and the plateau modulus (equations (2) and (4)). Similarly, the yield stress defining the phase boundary exhibits critical-like variation in both ϕ and U (equations (6) and (7)). Moreover, as shown in the micrographs in Fig. 2, the stress plays a similar role to ϕ and U . This suggests that ϕ , U and σ are valid control parameters, and that changes in any of them are equivalent. Additional support for this equivalence comes from the behaviour of the full frequency-dependent storage and loss moduli of solid-like samples, $G'(\omega)$ and $G''(\omega)$, which can be scaled onto identical master curves as either ϕ is varied and U is held fixed, or as U is varied and ϕ is held fixed. Similar scaling is observed for the nonlinear stress response as a function of shear rate for the solid-like samples¹⁰. Finally, both the divergence of the relaxation time of the clusters as gelation approaches, and the shape of the correlation function, are similar to the behaviour observed as the colloidal glass transition is approached, highlighting the equivalence of gelation and the glass transition as examples of the jamming transition¹¹.

An integral feature of the jamming transition is the concept of stress-bearing chains^{1,9}, which was introduced initially for granular systems, but has since been extended to other systems as well¹³. Attractive colloid systems might provide a useful system with which directly to probe these force chains; unlike more dense repulsive systems, the chains are directly visible as the tenuous colloidal network, with nearly all constituents being part of the stress-bearing structure. By contrast, in repulsive systems, force chains are difficult to observe, because they are obscured by the large number of spectator particles, which are not part of the stress-bearing structure. However, gelling systems show a characteristic divergence of the yield strain, γ_y , as the jamming phase boundary is approached, in contrast to granular systems, which are predicted to be fragile, implying a finite γ_y (ref. 9). The differences in behaviour of the two classes of jammed systems merit further investigation.

Our results confirm that a phase diagram can be used to unify the description of a wide variety of transitions from fluid-like to solid-like behaviour by means of the jamming transition, providing striking confirmation of the proposal of Liu and Nagel². Moreover, our results justify the applicability of the jamming transition in describing systems with attractive interactions, significantly extending the range of materials to which these ideas apply. For practical applications, the jamming phase diagram provides important guidance in the parameters that should be changed to achieve a desired behaviour. We conclude by emphasizing that the concept of jamming is a powerful means to account for a wide range of fluid–solid transitions found in colloid systems and helps rationalize apparently diverse behaviour for very different systems; thus, the colloidal glass transition, colloidal gelation and aggregation can all be put on an equal footing as representations of the jamming transition. □

Received 16 January; accepted 30 April 2001.

1. Edwards, S. F. & Grinev, D. V. in *Jamming and Rheology: Constrained Dynamics on Microscopic and Macroscopic Scales* (eds Liu, A. J. & Nagel, S. R.) 80–93 (Taylor and Francis, New York, 2001).
2. Liu, A. J. & Nagel, S. R. Jamming is not just cool anymore. *Nature* **396**, 21–22 (1998).

3. Pusey, P. N. & van Meegen, W. Observation of a glass transition in suspensions of spherical colloidal particles. *Phys. Rev. Lett.* **59**, 2083–2086 (1987).
4. Grant, M. C. & Russel, W. B. Volume-fraction dependence of elastic moduli and transition temperatures for colloidal silica gels. *Phys. Rev. E* **47**, 2606–2614 (1993).
5. de Rooij, R., van den Ende, D., Duits, M. H. G. & Mellema, J. Elasticity of weakly aggregating polystyrene latex dispersions. *Phys. Rev. E* **49**, 3038–3049 (1994).
6. Weitz, D. A. & Oliveria, M. Fractal structures formed by kinetic aggregation of aqueous gold colloids. *Phys. Rev. Lett.* **52**, 1432–1435 (1984).
7. Carpinetti, M. & Giglio, M. Spinodal-type dynamics in fractal aggregation of colloidal clusters. *Phys. Rev. Lett.* **68**, 3327–3330 (1992).
8. Gisler, T. & Weitz, D. A. Strain hardening of fractal colloidal gels. *Phys. Rev. Lett.* **82**, 1064–1067 (1999).
9. Cates, M. E., Wittmer, J. P., Bouchaud, J. P. & Claudin, P. Jamming, force chains, and fragile matter. *Phys. Rev. Lett.* **81**, 1841–1844 (1998).
10. Trappe, V. & Weitz, D. A. Scaling of the viscoelasticity of weakly attracting particles. *Phys. Rev. Lett.* **85**, 449–452 (2000).
11. Segre, P. N., Prasad, V., Schofield, A. B. & Weitz, D. A. Glass-like kinetic arrest at the colloidal gelation transition. *Phys. Rev. Lett.* (in the press).
12. Pusey, P. N. & van Meegen, W. Phase behaviour of concentrated suspensions of nearly hard colloidal spheres. *Nature* **320**, 340–342 (1986).
13. O'Hern, C. J., Langer, S. A., Liu, A. J. & Nagel, S. R. Force distributions near jamming and glass transitions. *Phys. Rev. Lett.* **86**, 111–114 (2001).
14. Pusey, P. N., Pirie, A. D. & Poon, W. C. K. Dynamics of colloid polymer mixtures. *Physica A* **202**, 322–327 (1993).
15. Melrose, J. R. & Ball, R. C. The pathological behaviour of sheared hard spheres with hydrodynamic interactions. *Europhys. Lett.* **32**, 535–540 (1995).

Acknowledgements

We thank S. Nagel and A. Liu for valuable discussions, and for permission to reproduce Fig. 1. This work was supported by Infineum, the NSF and NASA.

Correspondence and requests for materials should be addressed to D.A.W. (e-mail: weitz@deas.harvard.edu).

Formation of chiral morphologies through selective binding of amino acids to calcite surface steps

C.A. Orme*, A. Noy*, A. Wierzbicki†, M. T. McBride*, M. Grantham‡, H.H. Teng§, P.M. Dove‡ & J.J. DeYoreo*

* Chemistry and Material Science Department, Lawrence Livermore National Laboratory, Livermore, California 94551, USA

† Department of Chemistry, University of South Alabama, Mobile, Alabama 36688, USA

‡ Department of Geological Sciences, Virginia Polytechnic Institute and State University, Blacksburg, Virginia 24061, USA

§ Department of Earth and Environmental Sciences, The George Washington University, Washington, District of Columbia 20052, USA

Many living organisms contain biominerals and composites with finely tuned properties, reflecting a remarkable level of control over the nucleation, growth and shape of the constituent crystals^{1–6}. Peptides and proteins play an important role in achieving this control^{1,7,8}. But the general view that organic molecules affect mineralization through stereochemical recognition, where geometrical and chemical constraints dictate their binding to a mineral, seems difficult to reconcile⁴ with a mechanistic understanding, where crystallization is controlled by thermodynamic and kinetic factors⁹. Indeed, traditional crystal growth models emphasize the inhibiting effect of so-called 'modifiers' on surface-step growth, rather than stereochemical matching to newly expressed crystal facets. Here we report *in situ* atomic force microscope observations and molecular modelling studies of calcite growth in the presence of chiral amino acids that reconcile these two seemingly divergent views. We find that enantiomer-specific binding of the amino acids to those surface-step edges that offer the best geometric and chemical fit changes the step-edge

free energies, which in turn results in macroscopic crystal shape modifications. Our results emphasize that the mechanism underlying crystal modification through organic molecules is best understood by considering both stereochemical recognition and the effects of binding on the interfacial energies of the growing crystal.

Growth of pure calcite, which has been investigated in detail by atomic force microscopy (AFM)¹⁰, yields rhombohedral crystals with six crystallographically equivalent {104} facets. The atomic steps on the crystal surfaces reflect this symmetry (Fig. 1a), with two steps acute to the {104} cleavage plane and two steps obtuse to the cleavage plane, forming a rhombus. The two obtuse steps are related through a glide-plane symmetry element, as are the two acute steps¹¹.

We monitored the effects of adding different amino acids to the solution from which calcite is grown. As shown in Fig. 1b, upon adding glycine, an achiral amino acid, the two acute steps become curved and lose their well defined facet directions, while the two obtuse steps are unaffected and the growth hillock retains its overall symmetry about the glide plane. Addition of an aqueous aspartic acid (Asp) solution also results in only the two acute steps becoming curved while the two obtuse steps remain unaffected. However, with the addition of only one of the two Asp enantiomers, D- or L-Asp, the symmetry about the glide plane is broken. The surface morphology depends on the chirality of the aspartic acid: growth hillocks formed in the presence of D- and L- forms of Asp are mirror images of one another (Fig. 1c and d). This Asp-induced change in surface morphology manifests itself also in the shape of so-called etch pits, which form when the crystal dissolves (Fig. 1e and f)¹². As the additive Asp has not been introduced into the bulk crystal, these effects must result from interactions between calcite and Asp at the surface step edges.

Some organic molecules are known to alter the habit of bulk crystals^{3,5,6,8,13,14}. To investigate how the changes in the atomic-scale configuration of surface steps illustrated in Fig. 1c–f might translate into bulk crystal habit alterations, we nucleated calcite in the presence of Asp. As illustrated by Fig. 1g and h, a new set of facets is expressed, and these lie approximately parallel to the {001} axis of pure calcite and map to the {hk0} family of planes. Three {104}

facets cap the {hk0} cylinder, with the shape of these cap facets matching almost exactly the shape exhibited by the calcite atomic steps seen in Fig. 1c and d. The obtuse steps, unaffected by Asp, form the straight ridges connecting the cap facets, while the curved acute steps form the rounded base of the cap. Changes in the shape of atomic steps can thus directly modify the macroscopic crystal shape of calcite, by inducing the formation of a new family of faces approximately parallel to the *c* axis.

Chiral molecules have been shown to reduce the symmetry of composite systems^{12,15–19}, and formation of homochiral surface facets upon adsorption of chiral amino acids has recently been

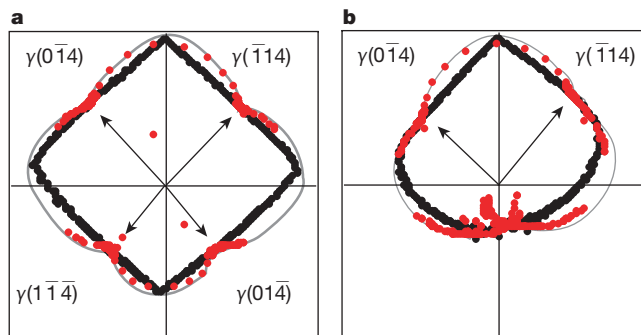


Figure 2 Orientational dependence of step-edge energy (two-dimensional Wulff plot) in the {104} plane. Plots are based on equilibrium crystal shapes for crystals grown in **a**, pure solution and **b**, 0.01 M D-Asp-bearing solution. The step shape is shown in black and the relative step-edge free energy γ calculated from these shapes is shown in red (with a grey line to guide the eye). The binding energy calculations predict that D-Asp will preferentially bind to the (014) riser over the (114) riser. The new minimum also appears in this quadrant. The two-dimensional Wulff plot for L-Asp-bearing solutions is the mirror image of **b**. The validity of assuming equilibrium crystal shapes in our system is supported by the similarity of the atomic-scale morphology of the growth hillock on the {104} facet to that of the bulk crystal, which suggests that the steps are indeed in their equilibrium geometry. Even hillocks grown in solutions with near-equilibrium CaCO₃ concentrations displayed this modified shape, as did the first turn of the spiral which is set by the energetics of the critical nucleus shape.

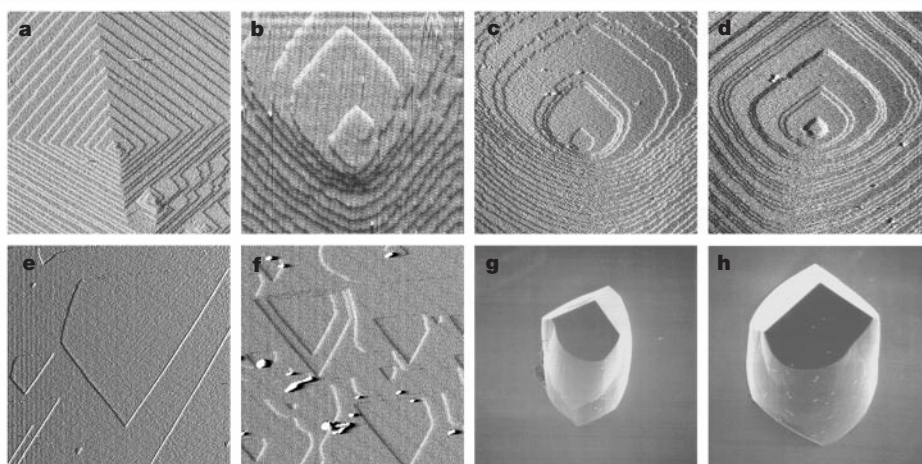


Figure 1 Images showing the effect of amino acids on calcite morphology. **a–f**, AFM images showing the effect of amino acids on growth-hillock and dissolution-pit geometry. **a**, A pure calcite growth hillock. **b–d**, Growth hillocks following addition of supersaturated solutions with 0.01 M glycine, an achiral amino acid (**b**); 0.01 M L-aspartic acid (**c**); and 0.01 M D-aspartic acid (**d**). **e, f**, Dissolution pits undersaturated with respect to calcite and saturated with respect to L- and D-Asp respectively. All images are shown in the same orientation as **a** with two obtuse steps at the top of the image. Image sizes are: **a**, 3.5 × 3.5 μm; **b**, 3 × 3 μm; **c** and **d**, 15 × 15 μm; **e**, 10 × 10 μm; and **f**, 5 × 5 μm.

g, h, SEM micrographs of calcite crystals nucleated on COOH-terminated regions of patterned self-assembled monolayers of alkane thiols³³ and grown in the presence of 0.01 M L-Asp and D-Asp respectively. The macroscopic crystals exhibit a columnar morphology with three {104} facets forming a cap at each end. The straight edges of these caps correspond to the obtuse steps that are the two steps in the upper half of the AFM images. The shape and chirality of each facet matches that of the growth hillocks shown in **c** and **d**. The curved surfaces that form the barrel of each column have general {hk0} orientations.

reported²⁰. Our observations, showing that breaking the symmetry of atomic steps leads to a reduced overall crystal symmetry and the emergence of chiral shapes, elucidates the interactions between chiral molecules and inorganic surfaces that give rise to these effects. Living organisms might use a similar mechanism to create the chiral morphology seen in many biomineralized structures^{13,18}.

Figure 2 shows polar plots of the free energies of the step edges on the {104} calcite facet (that is, two-dimensional Wulff plots²¹) constructed from the facet shapes (see Fig. 2 legend for details). The Wulff plot for pure calcite growth exhibits distinct minima along the four step directions (Fig. 2a). The hillock growing in the presence of Asp is much more isotropic near the three corners involving the acute steps; in the corresponding Wulff plot, the minima associated with the two acute step edges is eliminated, reflecting that the energetic cost of creating curvature—and therefore kink sites—is significantly diminished in this system. In addition, a new minimum appeared near the intersection of the glide plane with the two acute step edges, indicating that Asp addition generates a new low-energy orientation for the step. The minimum position switched from the right side of the glide plane to the left side upon changing the amino acid from D-Asp to L-Asp.

The addition of Asp at 2 to 200 times the CaCO₃ concentration had little or no effect on step-growth speeds, with only extremely high Asp concentrations (~2,000 times the CaCO₃ concentration) leading to significant inhibition. Although an altered step geometry (Fig. 1c and d) is eventually obtained, the step edge remains smooth even at these high impurity levels. These observations suggest that in

contrast to the effects of impurity species in many other systems (see ref. 23 for example), Asp molecules adsorbed on the calcite surface do not act as pinning sites for step motion that would affect the growth kinetics. For additives that incorporate into the bulk, such as magnesium²³, the step velocity is strongly dependent on the additive concentration. Asp does not show such behaviour and therefore it is unlikely that Asp incorporates into the bulk of calcite crystal. Some kinetic effects may play a role, but the consistency in step shape over time and from the first turn of the spiral to the macroscopic shape, and the results of our step velocities measurements, all argue that growth is altered primarily by changing the energetics at the step edge.

Using X-ray photoelectron spectroscopy (XPS)²⁴ and surface X-ray diffraction^{25–27}, no evidence for Asp either on the {104} face or within the bulk of the crystal was observed, and the coverage of Asp on the {104} face and its abundance within the bulk is thus minimal ($\leq 0.3\%$). This finding might be taken to suggest that the effect of Asp on the {104} step morphology is due solely to its interaction with the steps, whose surface density never exceeded ~1%. However, typically only 0.02% protein is occluded in biogenic calcite skeletal elements, and similar occlusion levels have been found in synthetic calcite with altered morphology²⁸.

The chiral nature of the observed interaction implies that Asp binding to the calcite surface spans the chiral centre of the amino acid. Moreover, if the binding was localized at only one surface site, an identical binding position could be found on the opposite side of the glide plane that, by definition, exhibits mirror symmetry (Fig. 3). Consequently, an individual amino acid molecule must interact with at least two sites on the calcite face to exhibit chiral binding. Finally, lack of evidence for significant amounts of Asp on the {104} faces implies that the interaction only occurs at the step edges, and that it is the structure of these step edges that is modified and results in the expression of near-{hk0} faces.

Similar bidentate substitutional bonding to calcite {hk0} faces has been proposed⁵ for molecules having two carboxyl groups (which includes Asp), with binding geometries on the {110} faces that are in general agreement with our results. However, our AFM data clearly show that surface growth occurs on single steps, even in the presence of the amino acids, implying that acidic amino acids do not bind to a single {hk0} crystallographic plane during growth, but rather at the step edges. Furthermore, because two-site binding is necessary to explain chiral effects, the Asp–calcite complex must involve sites on both the step riser and the terrace.

We have calculated the binding energy of L- and D-Asp to the {104} face as well as to the acute step risers of single and double steps in the presence of water^{29–32}. The results predict that binding of Asp to the flat {104} surfaces of calcite involves all charged groups of the molecule. As shown in Table 1, there is no energy difference for binding of the D- and L- forms of Asp to the (104) surface of calcite, because both adsorbates can rotate to maximize their binding energy.

The binding geometry of Asp to the acute steps reflects the mirror symmetry of these steps and the chirality of the adsorbate (Fig. 3). (For simplicity we discuss only the binding of D-Asp to the acute steps, with the understanding that the discussion for L-Asp is equivalent but with the opposite acute step.) As shown in Fig. 3, on the cleavage plane, D-Asp binds to the (014) riser so that one of

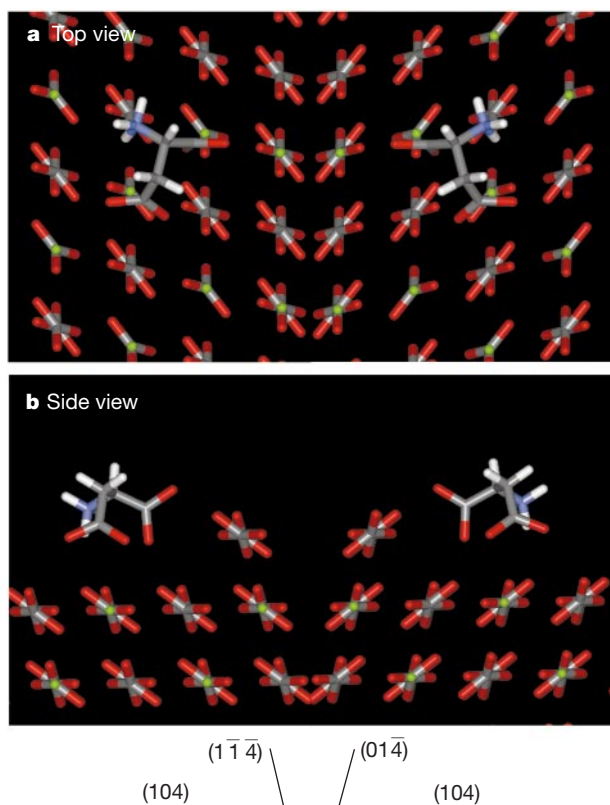


Figure 3 Geometry of binding for aspartic acid adsorbed on the single (104) steps of calcite. **a**, Top view and **b**, side view of L-Asp (left) and D-Asp (right) binding to the steps of calcite with (1 $\bar{1}$ 4) risers and (014) risers, respectively. The crystal surfaces are rotated and aligned to show the mirror symmetry of binding. Surfaces are viewed along the direction that aligns the calcium ions (small green spheres) with the centres of carbonate ions. Only fragments of the surface used for the modelling are shown. The following atom colouring scheme was used: calcium, green; carbon, grey; oxygen, red; nitrogen, blue; and hydrogen, white.

Table 1 Binding energies of D- and L-aspartic acid to the flat and stepped {104} surfaces of calcite

	(104)	104 single-step (014) riser	104 single-step (1 $\bar{1}$ 4) riser	104 double-step (014) riser	104 double-step (1 $\bar{1}$ 4) riser
D-Asp	-34.7	-41.0	-33.1	-49.4	-41.4
L-Asp	-34.3	-32.2	-41.4	-42.3	-49.8

Energies are expressed in units of kJ mol⁻¹. The binding energies were calculated using a dielectric constant of 80.

its negatively charged carboxyl groups (COO^-) completes the coordination of calcium ions while keeping the positively charged group (NH_3^+) in registry with positive ions at the surface. At the step, the remaining carboxyl group can bind to the two $\{104\}$ surfaces converging at the step, thus constraining the binding geometry and increasing the binding energy by approximately 19%, relative to that of binding to the cleavage plane. On the $(1\bar{1}\bar{4})$ riser, the carboxyl group of D-Asp matched the carbonates of the calcite only poorly; moreover, the group cannot rotate freely to optimize coordination, and the binding energy to the step is therefore slightly lower than to the flat cleavage plane.

When modelling the hypothetical case of Asp binding to double acute steps, we find that D-Asp is again bound more strongly to the $(01\bar{4})$ riser than to the $(1\bar{1}\bar{4})$ riser. But a better stereospecific fit to the double step increases the binding energy by approximately 40%, compared to binding to single acute steps on the (104) surface (Table 1). Double steps are not available during growth from dislocation hillocks, but as the steps reach the periphery of each (104) facet, they merge to form the adjacent facet and binding to double steps should become possible. Furthermore, the Asp double-step structure generates pseudo- $\{hk0\}$ step risers, from which the $\{hk0\}$ -like surfaces of the bulk crystals are likely to have emerged. These model calculations thus emphasize the energetic basis for the observed morphological changes induced by the presence of Asp during crystal growth.

Our results suggest that the addition of organic growth modifiers alters the energy landscape seen by adsorbing and desorbing calcite species at the surface of the mineral, thus changing the rates of attachment and detachment and/or the surface configuration that is lowest in energy. In particular, we find that site-specific binding of amino acid residues to surface steps changes the step-edge free energies, giving rise to direction-specific binding energies unique to individual amino acid enantiomers and leading to chiral modifications that propagate from atomic length scales to macroscopic length scales. Although stereochemical recognition describes the structural and chemical relationships present during the mineralization process, our findings indicate that the mechanism underlying crystal modification is better understood by considering surfactant-mediated changes to interfacial energies. □

Methods

Solutions and sample preparation

Supersaturated CaCO_3 solutions were prepared using reagent grade NaCl, NaHCO_3 , and $\text{CaCl}_2 \cdot 2\text{H}_2\text{O}$. Saturation ratios (S , defined below) ranged from 1.2 to 3, ionic strength 0.01 M, and $\text{pH} = 8.1$ – 8.6 . Solutions with amino acid additives (10^{-5} – 10^{-2} M) were readjusted for pH. Samples used for XPS and SXRD were prepared by overgrowth on cleaved geologic calcite (Brazil) similar to the AFM experiments. Patterned self-assembled monolayers of mercaptohexadecanoic acid and hexadecanethiol were fabricated on Au-coated (20 \AA of Ti, 750 \AA of Au) Si substrates using microcontact printing with an elastomeric stamp³³. The patterned substrates were placed monolayer side down on plastic standoffs into supersaturated calcium carbonate solutions sealed from the atmosphere. This placement ensured that only the crystals that nucleated directly on the film remained on the film. After two days the substrates were taken out of the solution and imaged by SEM. $S = a(\text{Ca}^{2+})a(\text{CO}_3^{2-})/K_{\text{sp}}$, where $a(\text{Ca}^{2+})$ and $a(\text{CO}_3^{2-})$ are the activities of the calcium ion and carbonate ion respectively and K_{sp} is the solubility constant for calcite.

Imaging

Atomic force microscopy (AFM) images were taken in contact mode using a Digital Instruments Nanoscope IIIa AFM equipped with a fluid cell. All images were obtained in solution under flowing conditions. High flow rates ($\sim 1 \text{ ml min}^{-1}$) were chosen to ensure surface kinetics were not affected by diffusion limitations. Some step-angle distortion occurred, owing to step-edge migration during the scan time. The images shown are not corrected for this. However, numerical data were corrected for the Doppler shifts by correlating successive images captured in the down and up scan direction. To minimize this effect, typical scan rates were 10 lines per second and thus had a scan time of approximately 50 s per image. Care was taken to ensure that the tip was not modifying the surface during the scan. For example, repeated scanning of the tip over the same point did not cause any appreciable differences at that location relative to the rest of the image. No local erosion or local enhancement of step velocities was observed. At the highest concentrations of Asp tested (0.1 M), lightly bound precipitates formed on the terraces because the Asp was supersaturated; these could be swept away with the tip motion.

X-ray photoelectron spectroscopy (XPS)

X-ray photoelectron spectra were measured using a Perkin-Elmer 5400 ESCA system equipped with a Mg X-ray source (Mg $K\alpha$ 1253.5 eV). Spectra were recorded using a concentric hemispherical analyser in the on-top position of the chamber, giving an overall energy resolution of 1.1 eV. Survey scans (89.5 eV pass energy, 1 eV step size) and high-resolution XPS spectra (17.90 eV pass energy, 0.1 eV step size) were acquired to determine surface compositions. Calcite and Asp both contain carbon and oxygen; therefore, we used the N 1s photoemission line as a fingerprint to establish the presence or absence of Asp on calcite surfaces. XPS has a detection sensitivity of 0.3 atomic per cent or about 0.5 weight per cent. The kinetic energy of the N 1s core electron is 850 eV, which corresponds to an escape depth of about 10 Å. Thus, the probability of an electron escaping from a N atom, and reaching the detector, from a depth of 10 Å is $1/e$, or about 37%; from a depth of 20 Å, the probability is $(1/e)^2$, or about 13.5%.

Surface X-ray diffraction (SXRD)

X-ray reflectivity measurements were performed at bending-magnet station 1-BM (SRI-CAT) of the Advanced Photon Source at Argonne National Laboratory. The basic principles of the technique have been described elsewhere^{25,27}. Crystals were mounted in a custom X-ray reflectivity cell (P. Fenter, M.T.M., G. Srajer, N.C. Sturchio & D. Bosbach, manuscript in preparation), bathed in about 1 ml of mother liquor. Experiments were performed in a static thin-film configuration with a water layer having a typical thickness of about 60 μm at the calcite surface contained by an 8- μm Kapton film. Each data set was measured in less than 2 h. A monochromatic X-ray beam ($\lambda = 0.775 \text{ \AA}$; photon energy, 16 keV) was incident upon the surface at a small angle, α (defined with respect to the surface plane), and the incident and reflected photon fluxes were measured separately as a function of α . Typical incident X-ray flux was about 10^{10} photons per second. X-ray reflectivity measurements were performed to a momentum transfer of $Q_{\text{max}} \approx 4 \text{ \AA}^{-1}$ resulting in a resolution of about 1.5 Å. This provides a simple estimate for the length scale over which the structure can be determined uniquely.

Molecular docking

Monovalent ions of D- and L-Asp were constructed using Spartan software for electronic calculations (Spartan 5.1.1 from Wavefunction Inc., of Irvine, California) and their geometries were optimized using the PM3²⁹ semi-empirical method. Corrections for aqueous solvation were applied using the Cramer–Truhlar SM3 solvation model^{30,34,35}. Electrostatic charges were assigned using the method of fitting to molecular electrostatic potentials^{31,32}. Flat and stepped calcite surfaces were built using Cerius² (from Molecular Simulations Inc., of San Diego, California) Surface Builder (Version 4.2MS) with the crystal surfaces charges assigned using Cerius². Energy minimizations were performed using the Universal Force Field 1.02 with dielectric constant equal to 80 to account for the water solvation effect. Binding energies were obtained by subtracting from the optimized energy of the adsorbate-surface system the energies of the surface and the adsorbate, when separated beyond the interaction distance.

Received 8 January; accepted 5 April 2001.

- Mann, S. *et al.* Crystallization at inorganic-organic interfaces—biominerals and biomimetic synthesis. *Science* **261**, 1286–1292 (1993).
- Addadi, L., Moradian, L. J., Shay, E., Maroudas, N. G. & Weiner, S. A chemical model for the cooperation of sulfates and carboxylates in calcite crystal nucleation—relevance to biomineralization. *Proc. Natl Acad. Sci. USA* **84**, 2732–2736 (1987).
- Sikes, C. S., Yeung, M. L. & Wheeler, A. P. in *Surface Reactive Peptides And Polymers: Discovery And Commercialization* (eds Sikes, C. S. & Wheeler, A. P.) ACS Symposium Series 444, Ch. 5, 50–71 (ACS Books, Washington DC, 1991).
- Mann, S. *et al.* Crystallization at inorganic-organic interfaces—biominerals and biomimetic synthesis. *Science* **261**, 1286–1292 (1993).
- Mann, S., Didymus, J. M., Sanderson, N. P., Heywood, B. R. & Samper, E. J. A. Morphological influence of functionalized and non-functionalized D-alpha,omega-dicarboxylates on calcite crystallization. *J. Chem. Soc. Faraday Trans.* **86**, 1873–1880 (1990).
- Berman, A., Addadi, L. & Weiner, S. Interaction of sea urchin skeleton macromolecules with growing calcite crystals—a study of intracrystalline proteins. *Nature* **331**, 546–548 (1988).
- Berman, A. *et al.* Biological control of crystal texture—a widespread strategy for adapting crystal properties to function. *Science* **259**, 776–779 (1993).
- Belcher, A. M. *et al.* Control of crystal phase switching and orientation by soluble mollusc-shell proteins. *Nature* **381**, 56–58 (1996).
- Burton, W. K., Cabrera, N. & Frank, F. C. The growth of crystals and equilibrium structure of their surfaces. *Phil. Trans. R. Soc. Lond. A* **243**, 299–358 (1951).
- Teng, H. H., Dove, P. M., Orme, C. A. & DeYoreo, J. J. Thermodynamics of calcite growth: Baseline for understanding biomineral formation. *Science* **282**, 724–727 (1998).
- Reeder, R. J. in *Carbonates: Mineralogy And Chemistry* (eds Reeder, R. J. & Mineralogical Society of America) Vol. II, Ch. 1, 1–47 (Mineralogical Society of America, Washington DC, 1983).
- Honess, A. P. & Jones, J. R. *Etch figure Investigations with Optically Active Solvents*. Technical Paper 35, 667–721 (Pennsylvania State College, Mineral Industries Experimental Station, 1937).
- Aizenberg, J. *et al.* Biologically induced reduction in symmetry—a study of crystal texture of calcitic sponge spicules. *Chem. Eur. J.* **1**, 414–422 (1995).
- Didymus, J. M. *et al.* in *Mechanisms And Phylogeny Of Mineralization In Biological Systems* (eds Suga, S. & Nakahara, H.) 267–271 (Springer, Tokyo/New York, 1991).
- Weissbuch, I., Addadi, L., Lahav, M. & Leiserowitz, L. Molecular recognition at crystal interfaces. *Science* **253**, 637–645 (1991).
- Addadi, L. *et al.* A link between macroscopic phenomena and molecular chirality: crystals as probes for indirect assignment of absolute configuration of chiral molecules. *Topics Stereochem.* **16**, 1 (1986).

17. Madura, J. D. *et al.* Interactions of the D-form and L-form of winter flounder antifreeze peptide with the (201) planes of ice. *J. Am. Chem. Soc.* **116**, 417–418 (1994).
18. Didymus, J. M., Young, J. R. & Mann, S. Construction and morphogenesis of the chiral ultrastructure of coccoliths from the marine alga *Emiliania Huxleyi*. *Proc. R. Soc. Lond. Ser. B* **258**, 237–245 (1994).
19. Mann, S., Sparks, N. H. & Blakemore, R. P. Structure, morphology and crystal growth of anisotropic magnetite crystals in magnetotactic bacteria. *Proc. R. Soc. Lond. Ser. B* **231**, 477–487 (1987).
20. Zhao, X. Y., Zhao, R. G. & Yang, W. S. Scanning tunneling microscopy investigation of L-lysine adsorbed on Cu (001). *Langmuir* **16**, 9812–9818 (2000).
21. Wulff, G. Velocity of growth and dissolution of crystal faces. *Z. Kristallogr.* **34**, 449–530 (1901).
22. Land, T. A., Martin, T. L., Potapenko, S., Palmore, G. T. & De Yoreo, J. J. Recovery of surfaces from impurity poisoning during crystal growth. *Nature* **399**, 442–445 (1999).
23. Davis, K. J., Dove, P. M. & De Yoreo, J. J. The role of Mg^{2+} as an impurity in calcite growth. *Science* **290**, 1134–1137 (2000).
24. Stipp, S. L. & Hochella, M. F. Structure and bonding environments at the calcite surface as observed with x-ray photoelectron spectroscopy (XPS) and low energy electron diffraction (LEED). *Geochim. Cosmochim. Acta* **55**, 1723–1736 (1991).
25. Feidenhansl, R. Surface structure determination by X-ray diffraction. *Surf. Sci. Rep.* **10**, 105–188 (1989).
26. Fenter, P. *et al.* Surface speciation of calcite observed in situ by high-resolution X-ray reflectivity. *Geochim. Cosmochim. Acta* **64**, 1221–1228 (2000).
27. Robinson, I. K. X-ray crystallography of surfaces and interfaces. *Acta Crystallogr. A* **54**, 772–778 (1998).
28. Albeck, S., Aizenberg, J., Addadi, L. & Weiner, S. Interactions of various skeletal intracrystalline components with calcite crystals. *J. Am. Chem. Soc.* **115**, 11691–11697 (1993).
29. Stewart, J. J. P. Optimization of parameters for semiempirical methods. 2. Applications. *J. Comput. Chem.* **10**, 221–264 (1989).
30. Cramer, C. J. & Truhlar, D. G. An scf solvation model for the hydrophobic effect and absolute free energies of aqueous solvation. *Science* **256**, 213–217 (1992).
31. Breneman, C. M. & Wiberg, K. B. Determining atom-centered monopoles from molecular electrostatic potentials—the need for high sampling density in formamide conformational analysis. *J. Comput. Chem.* **11**, 361–373 (1990).
32. Chirlian, L. E. & Francl, M. M. Atomic charges derived from electrostatic potentials—a detailed study. *J. Comput. Chem.* **8**, 894–905 (1987).
33. Aizenberg, J., Black, A. J. & Whitesides, G. M. Control of crystal nucleation by patterned self-assembled monolayers. *Nature* **398**, 495–498 (1999).
34. Cramer, C. J. & Truhlar, D. G. General parameterized scf model for free energies of solvation in aqueous solution. *J. Am. Chem. Soc.* **113**, 8305–8311 (1991).
35. Cramer, C. J. & Truhlar, D. G. Am1-Sm2 and Pm3-Sm3 parameterized scf solvation models for free energies in aqueous solution. *J. Computer-Aided Molecul. Design* **6**, 629–666 (1992).

Acknowledgements

We thank S. Zepeda, S. Orme and J. Beringer for assistance with AFM data collection, P. Fenter for performing the SXRD studies, A. Nelson and C. Evans for help with XPS, S. Sikes for helpful discussions and L. Addadi for a careful reading of the manuscript. This work was performed under the auspices of the US Department of Energy by Lawrence Livermore National Laboratory and was supported by a grant to Georgia Institute of Technology from the Division of Geosciences and Engineering, Office of Basic Energy Sciences, Department of Energy.

Correspondence and requests for materials should be addressed to C.O. (e-mail: orme1@llnl.gov).

Evidence for fault weakness and fluid flow within an active low-angle normal fault

J. S. Floyd*, J. C. Mutter*†, A. M. Goodliffe‡ & B. Taylor‡

* Lamont-Doherty Earth Observatory, Columbia University, Palisades, New York 10964; and Department of Earth and Environmental Sciences, Columbia University; and † Columbia Earth Institute, Columbia University, New York 10027, USA

‡ School of Ocean and Earth Science and Technology, University of Hawaii, Honolulu, Hawaii 96822, USA

Determining the composition and physical properties of shallow-dipping, active normal faults (dips < 35° with respect to the horizontal) is important for understanding how such faults slip under low resolved shear stress and accommodate significant extension of the crust and lithosphere. Seismic reflection images¹ and earthquake source parameters² show that a magnitude 6.2 earthquake occurred at about 5 km depth on or close to a

normal fault with a dip of 25–30° located ahead of a propagating spreading centre in the Woodlark basin. Here we present results from a genetic algorithm inversion of seismic reflection data, which shows that the fault at 4–5 km depth contains a 33-m-thick layer with seismic velocities of about 4.3 km s⁻¹, which we interpret to be composed of serpentinite fault gouge. Isolated zones exhibit velocities as low as ~1.7 km s⁻¹ with high porosities, which we suggest are maintained by high fluid pressures. We propose that hydrothermal fluid flow, possibly driven by a deep magmatic heat source, and high extensional stresses ahead of the ridge tip have created conditions for fault weakness and strain localization on the low-angle normal fault.

We use multichannel seismic (MCS) reflection data acquired aboard the RV *Maurice Ewing* during a 1995 survey and drilling results from Ocean Drilling Program (ODP) Leg 180 (refs 3 and 4; Fig. 1). MCS profiles^{1,4} reveal a normal fault that maintains a dip of 25–30° to about 9 km depth and an offset of 10–12 km between the sedimented hanging wall and the Moresby seamount footwall, which is composed of Palaeocene arc-ophiolite gabbro and dolerite^{3,5}. Faulting and uplift of Moresby seamount is estimated to have begun within the last 3.5 Myr, based on the first occurrence of metamorphic talus found in the downdropped hanging wall at ODP Site 1108 and an abrupt increase in sedimentation rate that indicates rapid subsidence of the northern margin at this time³. This fault is one of the major structures on which continental extension appears to be localized. The close proximity of the fault to the

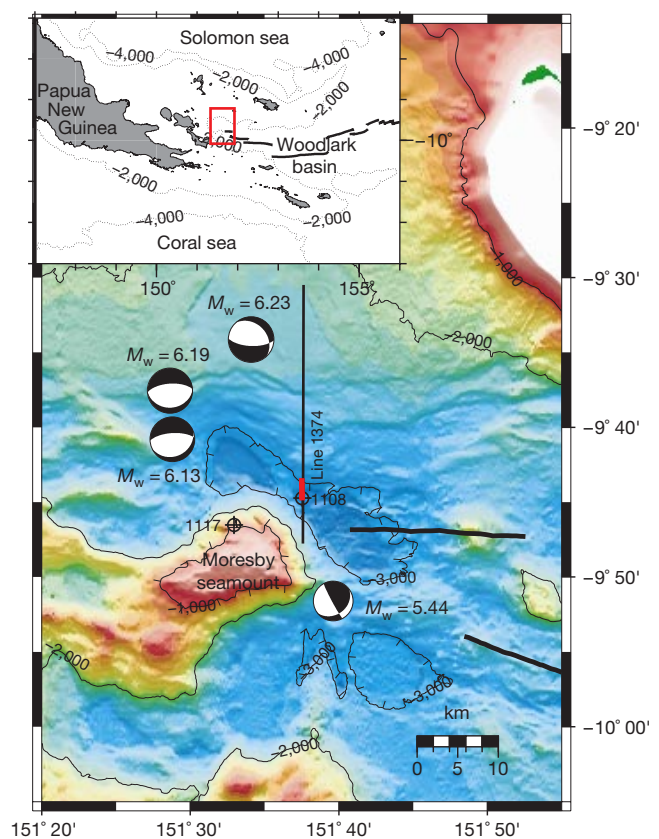


Figure 1 Bathymetry map of the study area showing the location of RV *Maurice Ewing* EW9510 multichannel seismic (MCS) reflection line 1374. The portion of the MCS line 1374 used in the inversion is marked in red. The ODP Leg 180 drill sites 1108 and 1117 discussed in the text are marked³. Earthquake focal mechanisms² shown include the M_w 6.23 event which occurred on or near the low-angle normal fault on the northern flank of Moresby seamount. Heavy black lines mark the location of the ridge axis interpreted from side-scan sonar data²³. Bathymetry contours are given in units of metres. Inset, regional map showing the location of the study area (red box).